Research Square

Preprints are preliminary reports that have not undergone peer review.
They should not be considered conclusive, used to inform clinical practice,
or referenced by the media as validated information.

Macroscopic and controlled levitation by photoelectric conversion

Metin Sitti

sitti@is.mpg.de

Max Planck Institute for Intelligent Systems https://orcid.org/0000-0001-8249-3854

Dalei Wang

Soochow University

Changsong Zhan

Soochow University

Chenjun Chu

Soochow University

Mingtong Li

Max Planck Institute for Intelligent Systems https://orcid.org/0000-0002-1685-6052

Haochen Huang

Soochow University

Hao Yang

Soochow University https://orcid.org/0000-0002-8241-6231

Lei Liu

Southeast University

Xinjian Fan

Soochow University

Zhen Hou

Soochow University

Zijun Ye

Soochow University

Jun Zhong

Soochow University https://orcid.org/0000-0002-8768-1843

Tao Cheng

Soochow University https://orcid.org/0000-0003-4830-177X

Wenqi Hu

The Hong Kong University of Science and Technology https://orcid.org/0000-0002-3457-821X

Jiwei Jiang

Soochow University

Hui Zhang

Soochow University

Bin Dong

Soochow University https://orcid.org/0000-0001-5681-372X

Physical Sciences - Article

Keywords:

Posted Date: April 24th, 2026

DOI: https://doi.org/10.21203/rs.3.rs-9412121/v1

License: This work is licensed under a Creative Commons Attribution 4.0 International License.
Read Full License

Additional Declarations: There is **NO** Competing Interest.

Macroscopic and controlled levitation by photoelectric conversion

Dalei Wang[1]†, Changsong Zhan[1]†, Chenjun Chu[1]†, Mingtong Li[2]†*, Haochen Huang[1]†, Hao Yang[1]†, Lei Liu[3], Xinjian Fan[4], Zhen Hou[1], Zijun Ye[1], Jun Zhong[1], Tao Cheng[1], Wenqi Hu[5], Jiwei Jiang[1*], Hui Zhang[1*], Bin Dong[1*], Metin Sitti[6*]

[1]State Key Laboratory of Bioinspired Interfacial Materials Science, Institute of Functional Nano and Soft Materials Laboratory (FUNSOM), Jiangsu Key Laboratory for Carbon-Based Functional Materials & Devices, Soochow University, Suzhou, Jiangsu 215123, China

[2]Physical Intelligence Department, Max Planck Institute for Intelligent Systems, 70569 Stuttgart, Germany

[3]School of Mechanical Engineering, Southeast University, Nanjing 211189, China

[4]School of Mechanical and Electrical Engineering, Soochow University, No. 8, Jixue Road, Suzhou, 215131, China

[5]Department of Mechanical and Aerospace Engineering, The Hong Kong University of Science and Technology, Clear Water Bay, Kowloon, Hong Kong, China.

[6]School of Medicine and College of Engineering, Koç University, 34450 Istanbul, Turkey

†These authors contributed equally: Dalei Wang, Changsong Zhan, Chenjun Chu, Mingtong Li, Haochen Huang, Hao Yang

*Correspondence to: msitti@ku.edu.tr, bdong@suda.edu.cn, huizhang@suda.edu.cn, jwjiang@suda.edu.cn, mingtong@is.mpg.de

Abstract

Light-driven levitation in air has great potentials in a wide range of fields including aerospace, robotics, sensors and biology. However, achieving large-scale and precise manipulation at the same time remains a major challenge. In this work, we report the macroscopic and controlled levitation based on the photoconversion mechanism. Stable levitation of a variety of different photoelectric material, ranging from inorganic semiconductors (e.g., GaAs), organic semiconductors (e.g., PPy) to hybrid organic-inorganic semiconductors (e.g., PPy-TiO_2), low-dimensional materials (e.g., MoS_2), and even commercial chip such as GaN LED could be realized under white light illumination. The long time (> 7 min) levitation of macroscopic (> 1 cm × 1 cm ×1 mm) photoelectric materials relies on a fundamentally different mechanism that involves the light induced charge separation, electron diffusion, the contact electrification and the subsequent electrostatic repulsion. More intriguingly, controlled directional motion of the photoelectric material or commercial chips could be induced through symmetry breaking in structures or irradiation. This levitation not only enhances the size and control precision of in-air levitation but also provides a universal, non-contact strategy for manipulating photoelectric materials holding great promise for applications in sensors, controllable assembly of optoelectronic devices and robotics.

Introduction

Actuators are essential components in robotics[1-3], sensors[4,5], artificial muscles[6-8], and biomedical devices[9-13], as they convert external stimuli, including electrical[14], thermal[15], magnetic[16-18], pneumatic[19] and chemicals[20] into programmable mechanical motions, enabling functionalities such as shape morphing[21,22], locomotion[23,24], manipulation[25], and adaptive operation in complex environments[26,27]. Owing to its non-contact and frictionless nature, levitation in air is particularly attractive for a variety of applications ranging from transportation, containerless measurements to synthesis and biomedicine[28-30]. In-air levitation can be achieved using various energy fields, such as the magnetic[31,32], acoustic[33], electric fields[34] or light[35,36]. Among others, the light-driven levitation in air offers distinct advantages, including high spatial and temporal resolution, environmental friendliness and remote control, making it particularly attractive for application in the field of aerospace, robotics, high sensitivity sensors and cell manipulation[28,37-39]. However, current light-driven levitation approaches, optical tweezer or photophoresis, face challenges in realizing large-scale and precise manipulation at the same time. Optical tweezers, which rely on radiation pressure to achieve light-matter momentum exchange, can generate only piconewton-level forces and require tightly focused, high-intensity laser beams, limiting their applicability to nano and microscale objects[40-42]; on the other hand, photophoretic levitation, arising from light-induced thermal effect, can lift millimeter-sized objects, but its thermally induced nature makes the process sensitive to ambient environment and is thus challenging to control[43,44].

Photoelectric conversion lies at the core of modern information and energy technologies. Up till now, a wide range of photoelectric materials that are capable of photoelectric conversion have been developed which mainly include inorganic, organic, hybrid semiconductors and low-dimensional materials[45-48]. These materials, either pristine or blend, are brought in contact with each other or with the electrodes through microfabrication methods (vacuum deposition or spin coating) in a layer by layer or mixed fashion, forming junctions[49,50]. Under light irradiation, the charge separation occurs which the foundation of various applications in optoelectrical devices, for example, solar cells and photodetectors, in catalysts or in the biomedical field[51-54]. However, to the best of our knowledge, the photoelectric conversion mechanism has not been applied to the field of levitation.

In this work, we develop the macroscopic and controlled levitation based on the photoelectric conversion mechanism. This approach exhibits broad applicability across representative classes of photoelectric materials, including inorganic semiconductors (e.g., GaAs), organic semiconductors (e.g., PPy), hybrid organic-inorganic semiconductors (e.g., PPy-TiO_2), low-dimensional materials (e.g., MoS_2), and even commercial chips such as GaN LEDs. Under white-light irradiation, the in-air levitation arises from a fundamentally different mechanism other than momentum exchange or photophoresis that involves photogenerated charge separation, contact electrification and the resulting electrostatic repulsion. More interestingly, directional movement could be achieved when symmetry in either structure or irradiation is broken. We further demonstrate stable levitation by detecting ambient noise and propulsion behaviors by

assembling mini-LED chips/devices. The levitation strategy reported in the current study thus not only provides a universal pathway for the non-contact manipulation of photoelectric materials but also opens promising opportunities for controllable assembly of optoelectronic devices and sensors.

2. Results and Discussions

2.1 Concept of the white-light-driven levitation and propulsion system

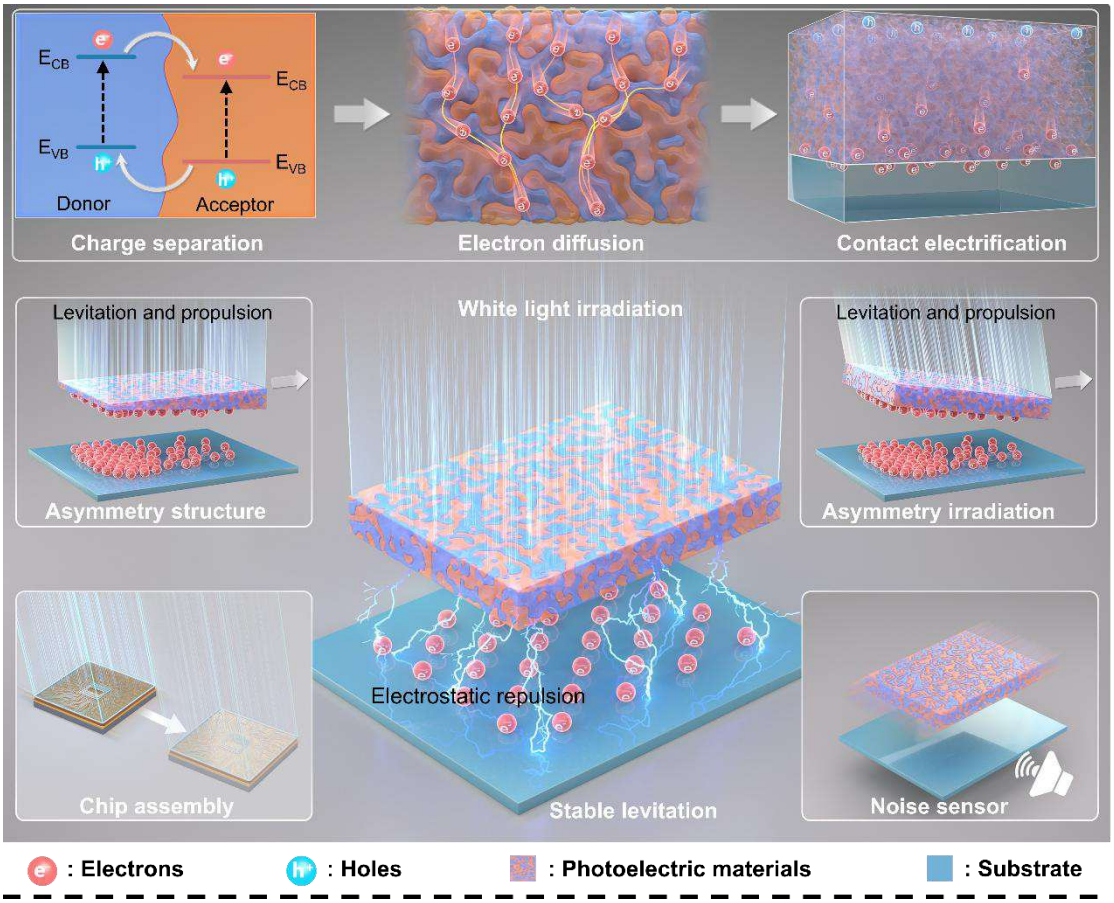


Fig. 1. White-light-driven levitation of the PPy-TiO_2 BHJ blend based on the photoelectric conversion mechanism. Schematic of photo-induced charge separation between electron donor and acceptor. Illustration of two independent donor and acceptor phases, where the blue and orange regions denote the electron donating and accepting material phases, respectively. Upon light irradiation on the top surface of the heterojunction, charge separation occurs at the donor-acceptor interface, followed by electron diffusion toward the bottom of the heterojunction blend. This process induces contact electrification and generates electrostatic repulsion, ultimately resulting in

levitation. Engineering illumination profile and the structural symmetry of the object can enable stable levitation behavior. Structural or illumination-induced asymmetries introduce non-equilibrium conditions, generating destabilizing forces or torques that produce unstable levitation and directional propulsion. Potential applications of the visible-light-driven heterojunction levitation, demonstrated in chip assembly and noise sensor.

We first take the PPy-TiO_2 bulk heterojunction (BHJ) blend as an example. As conceptually illustrated in Fig. 1, under light irradiation, the electron can be generated from the photoinduced charge separation of the heterojunction, which consists of an electron donor (PPy) and an electron acceptor material (TiO_2). The generated electron can be transported from the light illuminated upper to the bottom of the heterojunction due to the electron gradient. The energy level difference between the heterojunction and substrate causes the contact electrification between them, thus resulting in the electrostatic repulsion[55]. The mechanical stable levitation of the macroscopic heterojunction structures can be ensured through symmetric structural design in combination with tailored light illumination. In case the symmetry is broken either by the anisotropy in the shape of the heterojunction material or the incident light, an additional torque is generated that displaces from its equilibrium position or orientation, causing instable levitation and the resulting propulsion. This light levitation phenomenon enables precise monitoring of noise as well as positioning of commercial LED chips, showing great potential for practical applications.

2.2 White-light-driven levitation behavior of the PPy-TiO_2 BHJ blend

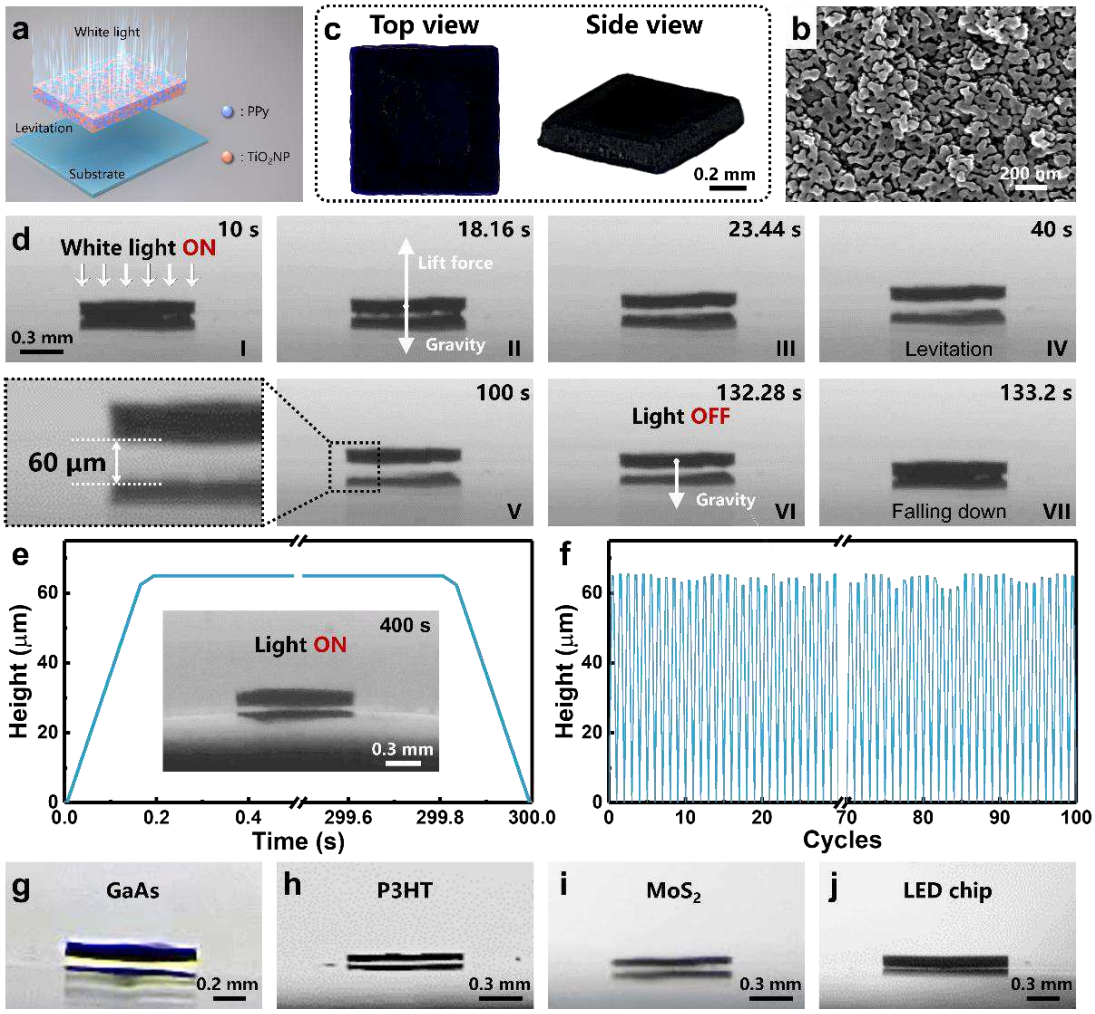


Fig. 2. The white-light-driven levitation of the PPy-TiO_2 BHJ blend in air. (a) The schematic illustration, (b) photograph image and (c) SEM image of the macroscopic PPy-TiO_2 BHJ structure. (d) The time-lapse images indicate the stable levitation process of the PPy-TiO_2 BHJ blend under visible light irradiation. (e) The levitation height versus the irradiation time of the PPy-TiO_2 BHJ blend. The insert image shows the levitation of the blend after 400 s visible light irradiation. (f) The repeatability of the visible-light-driven levitation of the PPy-TiO_2 BHJ blend. The images show the stable levitation behavior of different photoelectronic materials including (g) GaAs, (h) PPy, (i) MoS_2 and (j) commercial LED chip.

The PPy-TiO_2 BHJ consists arguably the simplest materials, the electron donating PPy and the electron accepting TiO_2, which are coupled together by blending (Fig. 2a-c). The PPy and TiO_2 form active complexes, where the charge separation is regulated by the application of external light. The PPy-TiO_2 BHJ blend is synthesized by the in-situ polymerization of pyrrole monomer in the presence of TiO_2NP (Supplementary Fig.

1). The fabrication, characterization and analysis of the PPy-TiO_2 BHJ blend is described in the *Method* section. As illustrated in Fig. 2d and Supplementary Video 1, the originally PPy-TiO_2 BHJ blend is statically placed on a printing paper (A4) substrate. When the visible light is applied vertically on its top surface, the PPy-TiO_2 BHJ blend levitates as evidenced by the air gap between the blend and the substrate (Fig. 2d). The PPy-TiO_2 BHJ blend takes around 112 ms to generate enough force to counteract its own gravity, initially lifting one side off the substrate, as shown in the Supplementary Fig. 2 and Supplementary Video 2. At the steady state, the blend can reach a levitation height as high as 60 μm (Fig. 2d). The long term and stable levitation can be achieved for over 7 min under continuous illumination (Fig. 2e and Supplementary Video 3). Once the irradiation is withdrawn, the blend falls back to the ground. Notably, the PPy-TiO_2 BHJ blend can achieve levitation at a macroscopic scale, with dimensions up to 1 cm × 1 cm × 1 mm (Supplementary Fig. 3 and Supplementary Video 4). The levitation process could be repeated for more than 100 times without noticeable deterioration in the levitation behavior (Fig. 2f). Furthermore, besides using PPy-TiO_2 BHJ blend as the main object of study, we have also explored the bulk heterojunction with other compositions. We investigated a series of blends with different donor-acceptor combinations, as shown in Supplementary Fig. 4, including PPy-ZnO, PPy-Cr_2O_3, PPy-Fe_2O_3 as well as Polyaniline-TiO_2 (PANI-TiO_2), Poly(3,4-ethylenethiophene)-TiO_2 (PEDOT-TiO_2), and Poly(3-hexylthiophene)-TiO_2 (P3HT-TiO_2). All of these bends are able to exhibit stable levitation behavior. In addition, we find that a wide range of photoelectronic materials, including inorganic semiconductors (GaAs, Fig. 2g), organic

semiconductors (PPy, Fig. 2h) and low-dimensional materials (MoS_2, Fig. 2i), can also realize levitation behavior under white-light irradiation. Remarkably, commercial GaN LED chips, which are planar heterojunction devices, are likewise capable of exhibiting levitation (Fig. 2j). The above results demonstrate the generality of light-driven strategy we reported.

2.3 Mechanism of visible-light-driven levitation in the PPy-TiO_2 BHJ blend

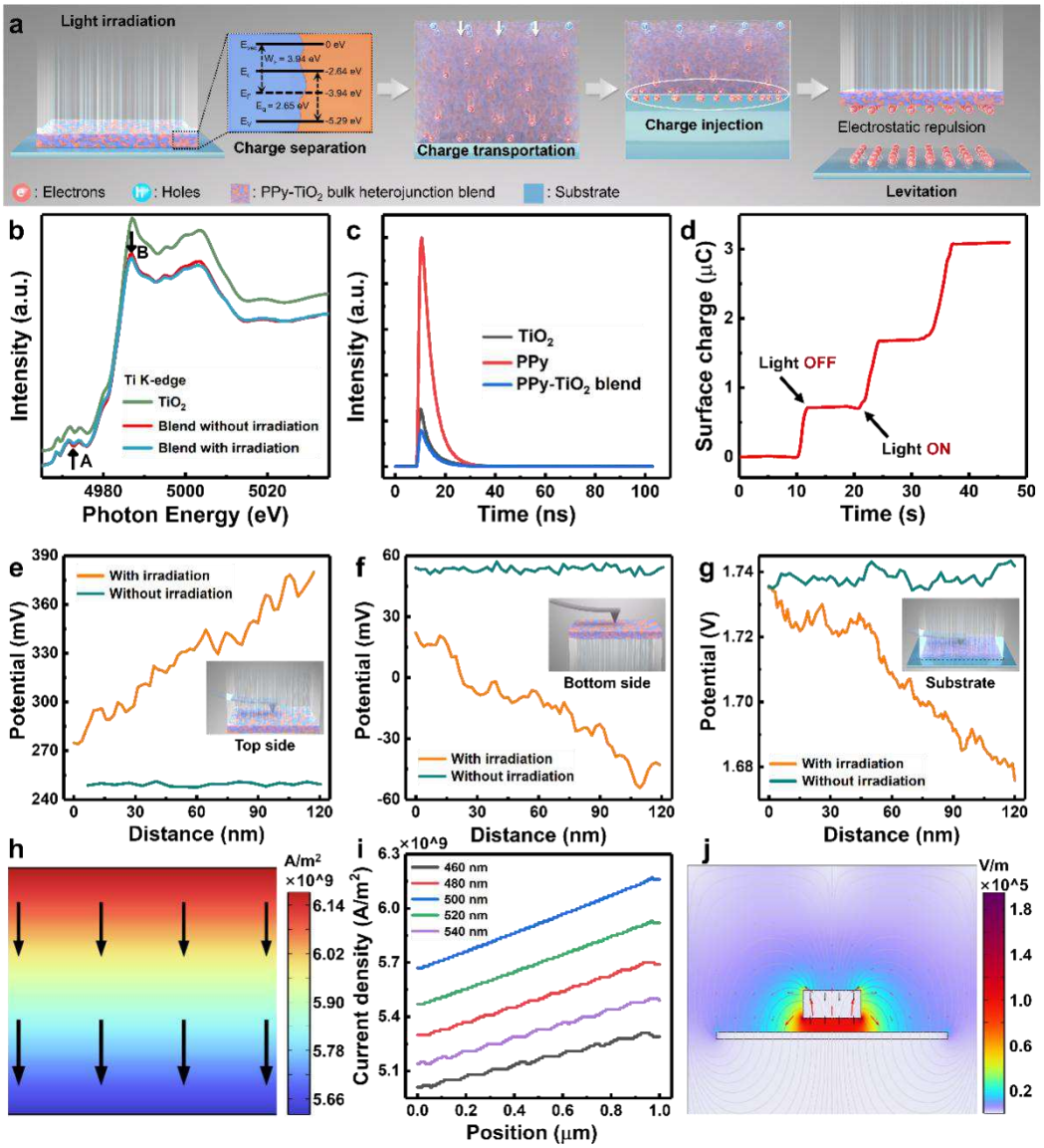


Fig. 3. Mechanism of the visible light-driven levitation in PPy-TiO_2 BHJ blend. (a) Schematic illustration of the levitation mechanism, including light-induced charge separation, charge transportation, charge injection, and electrostatic repulsion. (b) Ti K-edge XANES spectra of the pure TiO_2 (green), PPy-TiO_2 BHJ blend without irradiation

(red), and with irradiation (cyan). (c) PL spectrum of the PPy-TiO_2 BHJ blend under light irradiation. (d) Photocurrent measured from the non-irradiated bottom surface of the PPy-TiO_2 BHJ blend under top surface illumination. Surface potential changes of the (e) irradiated top surface, (f) non-irradiated bottom surface of the PPy-TiO_2 BHJ blend, and (g) substrate, with (red) and without (cyan) light irradiation. (h) Schematic illustration of the current density distribution under light irradiation used for the FEM simulation. (i) Simulated current density profile along the vertical direction from the top surface of the PPy-TiO_2 BHJ blend under irradiation at wavelength from 460 to 540 nm. (j) Simulated electrostatic repulsion force acting on the PPy-TiO_2 BHJ blend under illumination.

The white-light-driven levitation of the PPy-TiO_2 BHJ blend likely arises from a mechanism involving light-induced charge separation, transportation, injection and electrostatic repulsion (Fig. 3a). We have examined the mechanism by studying the blend's band structures using ultraviolet photoelectron spectroscopy (UPS) and UV-Vis-NIR spectroscopy, revealing the charge separation and diffusion through photoluminescence (PL) spectrum and photocurrent measurement, characterizing the contact electrification via kelvin probe force microscopy (KPFM), and supporting our findings with finite element method (FEM) simulation.

Among others, as indicated in the UPS and UV-Vis-NIR measurements, the PPy and TiO_2NP exhibit the highest occupied molecular orbital (HOMO) and energy gap (Eg) of -3.94 eV (HOMO)/3.94 eV (Eg) and -2.64 eV (HOMO)/2.65 eV (Eg), respectively. The band structure can thus be determined (Fig. 3a), indicating that the photogenerated electrons can transfer from the higher LUMO level of PPy to TiO_2NP. Under light irradiation, charge separation occurs on PPy, with electrons being injected from the LUMO of PPy into TiO_2NP. This electron transfer is evidenced by the increased absorption peak at 4792 eV (peak A in Fig. 3b, originating from Ti 1/2P) and the decreased absorption peak at 4986 eV (peak B in Fig. 3b, deriving from Ti 1/2P) in

the X-ray Absorption Near Edge Structure (XANES) measurement. These spectral changes indicate that TiO_2NP become electron rich, confirming the electron transfer. The charge separation in the PPy-TiO_2 BHJ blend is furthered confirmed by PL measurement. As shown in Fig. 3c, compared with pristine PPy and TiO_2, the PPy-TiO_2 BHJ blend shows reduced PL intensity and a faster time-resolved PL decay, indicating more efficient photoinduced charge generation and electron-hole separation in the heterojunction.

Due to the limited light penetration depth of approximately from 450 to 800 nm in the PPy-TiO_2 BHJ blend (Supplementary Fig. 5), charge separation occurs primarily in the irradiated top surface layers, creating an electron concentration gradient between the top and bottom surfaces. Consequently, electrons diffuse toward the bottom surface. This process is evidenced by the continuous photocurrent observed under constant light irradiation (Fig. 3d), confirming sustained electron transport within the blend. The photocurrent is measured using an electrometer, and the corresponding measurement setup is illustrated in Supplementary Fig. 6. The generation and diffusion of electrons in the blend are further confirmed by KPFM measurement. As shown in Fig. 3e-g, no surface potential is observed prior to light irradiation. However, upon illumination, the irradiated top surface exhibits an increased contact potential difference (CPD), while the non-irradiated bottom surface shows a decreased CPD. This observation verifies the proposed charge separation and diffusion mechanism: holes remain on the top surface due to their immobility within PPy, while mobile electrons diffuse toward the bottom surface. Interestingly, we also observe that the substrate (A4 paper) acquires a decreased

CPD. This is likely due to the contact electrification between the bottom surface of the PPy-TiO_2 BHJ blend and the substrate, resulting in a buildup of surface charge at the contact area. The resulting electrostatic repulsion between the negatively charged bottom surface and the substrate may contribute to the observed levitation behavior. Moreover, the charge on the substrate persists over time and dissipates slowly (Supplementary Fig. 7), enabling long-duration and stable levitation.

Next, to further validate the proposed mechanism, we perform numerical FEM simulations of the photoinduced charge generation, diffusion, and electrostatic-repulsion-driven levitation process (Fig. 3h-j). The detailed simulation procedures are described in the *Methods* section. As shown in Fig. 3h-i, under light irradiation, a high current density is observed near the illuminated top surface of the PPy-TiO_2 BHJ blend, indicating a high concentration of photogenerated charge carriers. These carriers subsequently redistribute and diffuse toward the bottom region. In addition, we utilize COMSOL Multiphysics simulations to estimate the resulting electrostatic repulsion force. As shown in Fig. 3j, the calculated repulsive force reaches approximately 2.21 μN, which agrees well with the experimentally estimated value of ~1.5 μN. The close agreement and consistent order of magnitude between simulation and experiment further support the validity of the proposed levitation mechanism.

2.4 Control of visible-light-driven levitation and propulsion of the PPy-TiO_2 BHJ blend

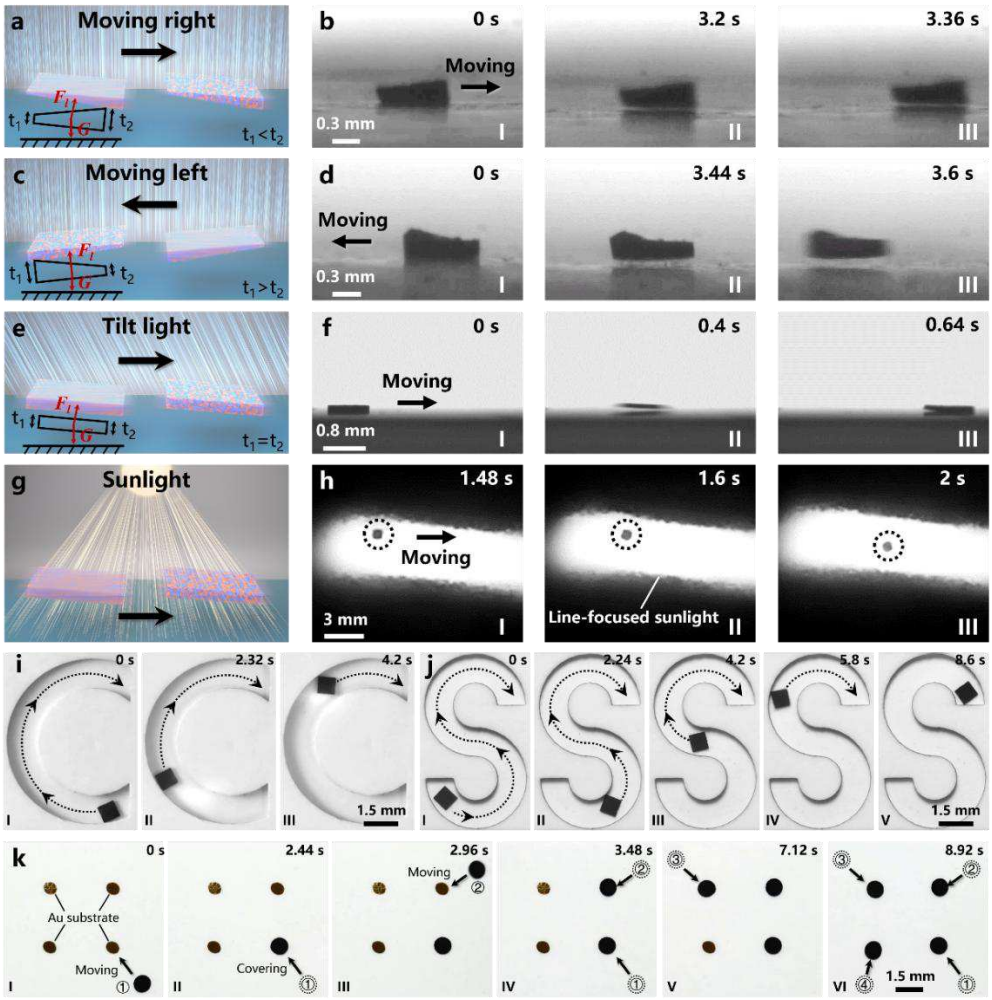


Fig. 4. Non-equilibrium condition-based levitation and propulsion. (a-d) Structural anisotropy in the PPy-TiO_2 BHJ blend leads to the non-equilibrium condition-based levitation and propulsion. (a,c) Schematic and (b,d) time lapse images show the rightward and leftward locomotion of the PPy-TiO_2 BHJ blend with a tapered thickness under vertically light irradiation. (a, b) and (c, d) correspond to films with increased thickness on the right and left sides, respectively, resulting in propulsion toward the thicker side. Anisotropy in light intensity distribution leads to an imbalance in levitation forces, driving directional motion. Under tilted light irradiation, the uniformly thick PPy-TiO_2 blend moves away from the light source due to asymmetric light-induced forces. The corresponding schematic and time lapse images are shown in (e) and (f), respectively. (g-h) Directional motion of the PPy-TiO_2 blend with a uniform thickness design under tilted sunlight irradiation. (i,j) Time-lapse images showing the motion of a PPy-TiO_2 BHJ blend confined within C-shaped and S-shaped grooves, respectively, following the corresponding C- and S-shaped trajectories under tilted light irradiation. (k) Time-lapse images illustrating the simultaneous light-driven coverage of four PPy-TiO_2 BHJ blends onto four Au substrates under tilted illumination.

The levitation behavior of the PPy-TiO_2 BHJ blend is influenced by several factors, including the substrate, irradiating light intensity and wavelength, thickness, and

material composition. We systematically optimized the levitation height of the PPy-TiO_2 BHJ blend under various parameter settings (see *Methods* section for details). Interestingly, introducing anisotropy into the structure or applying an asymmetric light intensity distribution disrupts the stable levitation state and can trigger directional propulsion. On the one hand, as shown in Fig. 4a-d, Supplementary Videos 5-6, when the PPy-TiO_2 blend with a tapered thickness (one side is thicker, which is synthesized by the template method) is subject to the vertical visible light irradiation, it levitates and moves toward the thicker side of the film. This behavior is mainly because the thinner side provides a shorter diffusion distance, enabling more efficient electron injection into the substrate. As a result, a stronger electrostatic repulsive force is generated on the thinner side, causing it to levitate at a higher altitude as compared to that of the thicker side (Supplementary Fig. 8). Consequently, the tapered PPy-TiO_2 blend is tilted, and the driving force is vertical to the tilted bottom surface. The component force parallel to the substrate thus leads to the propulsion in a direction along the thicker side of the film. We have also investigated the relationship between propulsive velocity and the thickness ratio on both sides. Based on the optimization experiment, the thickness of the thinner side of the composite film is fixed at 40 μm, while the thickness of the opposite side is systematically varied to modulate the thickness ratio. As shown in Supplementary Fig. 9, an increase in the thickness ratio leads to an enhancement in the propulsion velocity of the composite film, reaching a maximum speed of approximately 5 mm/s when the thickness ratio approaches 0.6.

On the other hand, as shown in Fig. 4e-f and Supplementary Video 7, when a tilted

light is applied on the surface of a PPy-TiO_2 BHJ blend with uniform thickness, it levitates and moves along a direction away from the light source, a behavior similar to the negative phototaxis. Under tilted irradiation, the top surface of the PPy-TiO_2 BHJ blend film is subjected to a non-uniform light intensity distribution, with regions closer to the light source receiving higher illumination and those farther away experiencing reduced intensity. As a consequence, the side under higher irradiation intensity could achieve a higher levitation height as opposed to the farther side under lower intensity light (Supplementary Fig. 10). The PPy-TiO_2 blend is also tilted, and the driving force is perpendicular to the tilted surface. The component force along the horizontal direction can thus propel the blend away from the light source. Additionally, the propulsion speed is dependent on the illumination angle. As can be seen from Supplementary Fig. 11, the propulsion speed is the fastest when the incident angle is 50º (the visible light intensity is fixed at 1 W/cm^2). Higher irradiation angles lead to less component force in the lateral direction, while lower angles may not generate light intensity strong enough to levitate the side farther to the light source. The low irradiation angle also results in lower repulsion force because the side wall of the composite film is illuminated in this case and becomes positively charged which causes less electron injection to the substrate. We have further explored the possibility of sunlight instead of xenon white light to achieve the levitation and propulsion of the PPy-TiO_2 BHJ blend. As shown in Supplementary Video 8, stable levitation can also be achieved under natural sunlight irradiation. As further demonstrated in Fig. 4g-h and Supplementary Video 9, we construct a linear light device to generate line-focused sunlight. The

asymmetric structured PPy-TiO_2 BHJ blend can achieve directional motion under such linear sunlight irradiation. Moreover, as shown in Supplementary Video 10, under tilted focused sunlight light irradiation, the levitation and propulsion of the PPy-TiO_2 BHJ blend is able to be achieved. The feasibility of sunlight as a driving light source for levitation greatly enhances the application prospects of our proposed levitation strategy.

Next, to further regulate the locomotion of the PPy-TiO_2 BHJ blend and achieve programmable trajectories, we have designed guiding tracks with different groove geometries (Fig. 4i-j), including C-shaped and S-shaped channels. By sequentially applying tilted illumination, the PPy-TiO_2 BHJ blend can be steered to follow well-defined C-shaped and S-shaped paths within these grooves, demonstrating controllable trajectory guidance through purely optical modulation (Supplementary Videos 11-12). Furthermore, the geometry of the PPy-TiO_2 BHJ blend is varied from square to circular. As shown in Supplementary Figs. 12-13 and Supplementary Videos 13-14, the circular samples exhibit similar guided motion within C-shaped and L-shaped channels under tilted illumination, indicating that the levitation and propulsion behavior is independent of the sample geometry. Additionally, because the propulsion mechanism is dominated by electrostatic repulsion, stable levitation and unstable propulsion cannot be achieved on conductive metal substrates, where rapid charge dissipation suppresses the generation of light-induced forces (Supplementary Fig. 7). Taking of this substrate-dependent behavior, we have fabricated a patterned substrate containing four circular Au pads. Under tilted illumination, the PPy-TiO_2 BHJ blend is driven across the surface and ultimately immobilized on the Au regions, forming a deterministic four-element

assembly pattern (Fig. 4k and Supplementary Video 15). Notably, compared with magnetic-field-based actuation, which often suffers from limited spatial selectivity and makes independent addressing of multiple objects within a confined microscale region challenging[9,17,56,57], optical control provides a highly localized and programmable stimulus, enabling scalable patterning and deterministic multi-object assembly.

2.5 Application of the light-induced levitation in the heterojunction.

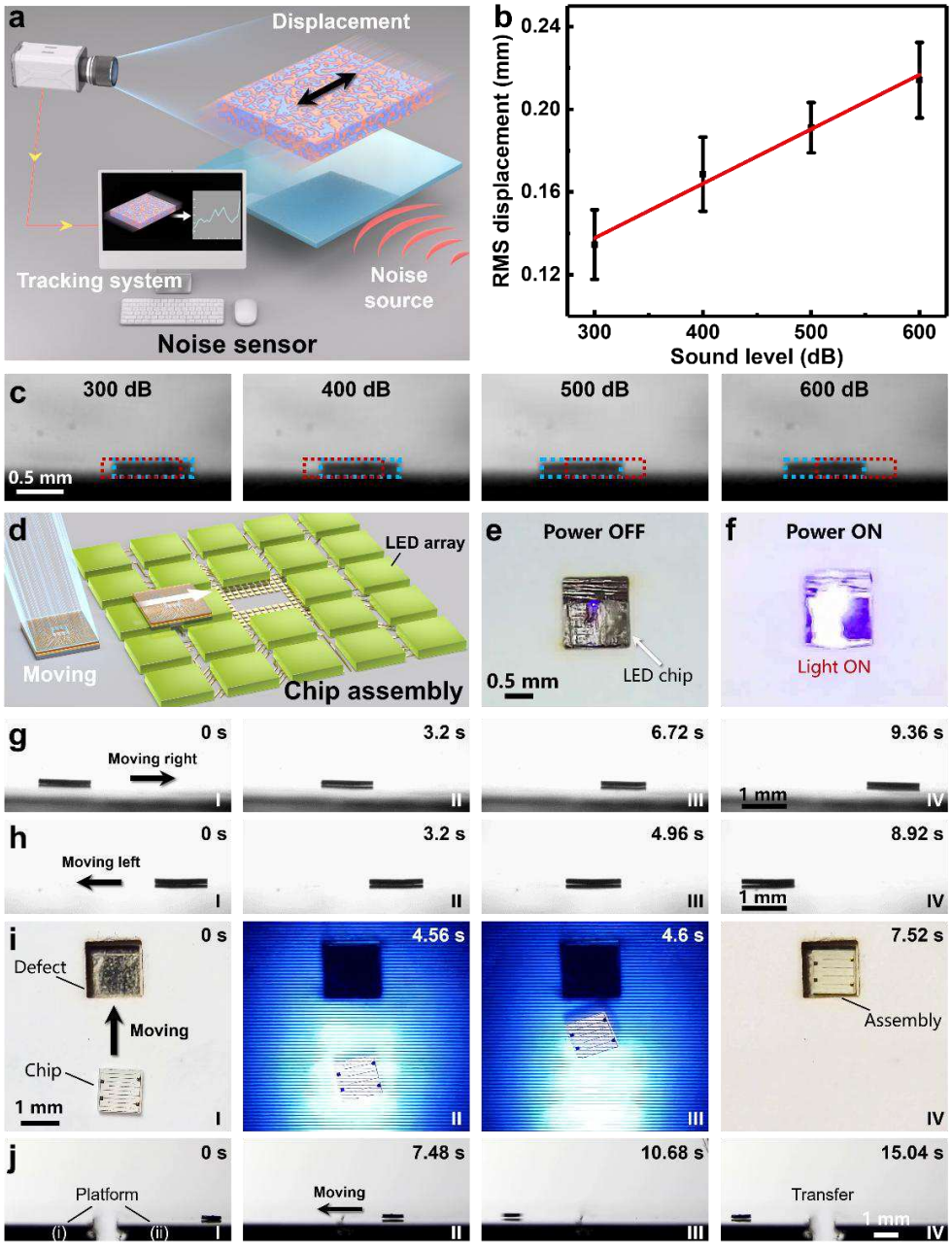


Fig. 5. Application demonstrations enabled by white-light-induced levitation. (a)

Schematic of the noise-sensing demonstration. Ambient noise levels are quantified by monitoring the RMS displacement of the levitated object under acoustic excitation with different sound-pressure levels (SPLs, dB). (b) RMS displacement of the levitated object as a function of SPL. The black curve represents measured values, and the red curve indicates the fitted trend. (c) Optical images showing the position shift of the levitated object under different SPLs. The blue box marks the initial position, and the red box indicates the displaced position. (d) Schematic illustrating light-driven manipulation of commercial chips for device assembly. (e, f) Photographs of the assembled LED device (e) before and (f) after powering on (i.e., without and with light emission). (g, h) Side-view time-lapse frames showing a commercial LED chip moving leftward (g) and rightward (h) under tilted light irradiation. (i) Top-view time-lapse frames showing a commercial LED chip driven under tilted illumination to fill a missing position in a device layout. (j) Side-view time-lapse frames showing light-driven transfer of the PPy-TiO_2 BHJ blend from platform ii to platform i.

We have demonstrated the feasibility and practical potential of the white-light-driven levitation phenomenon by developing several functional device prototypes, including a noise sensor and an accelerometer enabled by stable levitation, as well as a chip-assembly system enabled by unstable propulsion. The noise-sensing demonstration is shown in Fig. 5a-c and Supplementary Video 16. In this experiment, acoustic noise with different sound levels is applied around a stably levitated PPy-TiO_2 bulk BHJ film. The noise intensity is quantified by monitoring the displacement response of the levitated film and extracting its root-mean-square (RMS) displacement using a position-tracking system (Fig. 5a). As shown in Fig. 5b-c, the RMS displacement increases linearly with the sound level, yielding a correlation coefficient of 0.99485. These results indicate that the RMS displacement of the levitated PPy-TiO_2 BHJ film can serve as a quantitative metric for ambient noise detection. Compared with conventional mechanical vibration/acoustic sensors that rely on physical supports and electrical wiring, this levitation-enabled sensing scheme provides a contactless and electrically passive approach for acoustic detection, allowing remote optical readout

and offering intrinsic immunity to electromagnetic interference.

We have further explored the application potential of this white-light-induced stable levitation behavior for acceleration sensing. Based on the levitation mechanism revealed in this study, we have developed a light-driven levitation accelerometer consisting of a movable base platform, a uniform illumination field, and a PPy-TiO_2 bulk BHJ film (Supplementary Fig. 14 and Supplementary Video 17). Under illumination, the BHJ film levitates above the platform. When the platform undergoes acceleration, the levitating film tilts in the direction of moving (Supplementary Fig. 14a). This behavior arises from inertial effects: relative motion occurs between the base and the film, and the induced negative charges on the base interact electrostatically with the positively charged upper surface of the film. As a result, the film tilts toward the direction of base movement. The tilt angle correlates strongly with the magnitude of the acceleration, allowing for quantitative calibration. As shown in Supplementary Fig. 14b, experimental results show a linear relationship between tilt angle and acceleration with a correlation coefficient of 0.99627, indicating the high potential of this BHJ-based levitation mechanism for precision acceleration sensing applications. Levitation-based accelerometers are attracting increasing interest due to their high sensitivity, contactless operation, low noise, and excellent stability, making them promising for aerospace navigation, biomedical sensing, precision instrumentation, and quantum technologies[28,31,58,59]. Compared with conventional levitation accelerometers based on magnetic, electrostatic, or acoustic fields, our approach features a markedly simplified architecture and eliminates the need for bulky magnets, high-voltage electrodes, or

ultrasonic transducers. Moreover, both actuation and readout can be implemented purely optically, enabling wire-free operation and intrinsic immunity to electromagnetic interference. Importantly, the levitation condition can be conveniently tuned by adjusting the illumination, providing a straightforward route to reconfigurable sensitivity and dynamic range, and thereby expanding the applicability of this platform for precision sensing.

In the final demonstration, we apply this light-driven levitation strategy to contactless chip assembly (Fig. 5d). Conventional chip transport and placement methods, such as vacuum pick-and-place tools, electrostatic chucks (ESC), capillary bonding, flip-chip bonding, and microgrippers, typically rely on direct physical contact, which can introduce mechanical stress, contamination, or structural damage[60-63]. In addition, existing levitation-based manipulation approaches using magnetic or acoustic fields often require bulky hardware and are difficult to integrate into microscale packaging systems[64-66]. To address these limitations, we employ the levitation mechanism reported here for contactless manipulation of commercial chips. A commercial GaN LED chip is used as a model system, and the assembled device successfully emits light after electrical activation (Fig. 5e-f and Video 18). Notably, since GaN LED chips exhibit photoelectric characteristics, the chip also shows directional propulsion under tilted illumination (Fig. 5g-i, Supplementary Videos 19-21). After reaching the designated position, the chip remains intact without observable physical damage, and its functional integrity is further confirmed by stable light emission (Fig. 5e-f). Moreover, as shown in Fig. 5j and Supplementary Video 22, the

PPy-TiO_2 BHJ blend can be transferred between two platforms based on this levitation behavior: under tilted illumination, it moves from platform ii to platform i, further highlighting the potential of this approach for programmable chip transport and assembly. Overall, this contactless chip assembly strategy mitigates the risk of mechanical damage and provides a promising route toward next-generation semiconductor packaging and integration.

3. Conclusion

In this work, we report a visible-light-driven levitation and directional transport phenomenon under ambient conditions, based on the unique optoelectronic properties of photoelectric materials. Upon illumination, the photoelectric materials undergo photoinduced electron-hole separation, leading to the formation of a vertical charge gradient across the film. Electrons migrate toward the substrate and are injected into it, resulting in an electrostatic repulsion force that lifts the photoelectric materials into a stable levitating state. Using a PPy-TiO_2 BHJ blend as a model system, we demonstrate a stable levitation height of up to 60 μm and levitation durations exceeding 10 minutes. This behavior is highly repeatable, with stable levitation observed over hundreds of cycles. Furthermore, directional motion of the levitating film can be achieved either by introducing structural asymmetry into the photoelectric materials or by applying a non-uniform, inclined illumination. Notably, natural sunlight is also capable of inducing this directional motion, highlighting the practicality and scalability of the system. To evaluate the real-world applicability of the reported levitation mechanism, we have

further designed a light-driven levitating noise sensor, accelerometer, and applied the technique to a chip assembly process. These demonstrations confirm the versatility and functional potential of the photoelectric materials levitation strategy for applications in precision sensing and contactless microfabrication technologies.

4. Methods

4.2 Fabrication of the PPy-TiO_2 BHJ blend (Supplementary Fig. 1): 2 g of iron chloride (Sigma Aldrich Company) were first dissolved in 40 ml deionized water. 20 ml of the iron chloride solution were mixed with 5 ml of 20 nm TiO_2NP (Xuan Cheng Jing Rui New Materials Co. Ltd.) and stirred for 5 min. 200 µl of pyrrole (Sigma Aldrich Company) were then added into the above solution and stirred for 3 min. The resulting solution was centrifuged at 10000 rpm for 2 min. After removing the supernatant, the precipitate was re-dispersed in water. This process was repeated for three times to completely remove the unreacted materials. The final aqueous solution of PPy-TiO_2NP was drop-cast onto a template, followed by solvent evaporation under ambient conditions. The dried PPy-TiO_2 BHJ blend was used for the levitation and propulsion study.

4.2 Composition analysis of the PPy-TiO_2 BHJ blend: The blend contains 42 wt% PPy and 58 wt% TiO_2 (which corresponding to a volume ratio of 1:1), as characterized by the thermogravimetric analysis (TGA, Supplementary Fig. 15). The characteristic fourier-transform infrared (FTIR) spectroscopy peaks at 1180 cm^{-1} (-N-H bonds from PPy) and 400-800 cm^{-1} (stretching of Ti-O-Ti vibration from TiO_2) indicated the

presence of PPy and TiO_2NP inside the PPy-TiO_2 BHJ blend (Supplementary Fig. 16). The TiO_2NP inside the composite film has the form of anatase, as evidenced by the characteristic lattice spacing of 0.351 nm which corresponds to anatase TiO_2 (101), as shown in the high-resolution transmission electron microscopy (TEM) and the corresponding fast Fourier transformation (FFT) pattern (Supplementary Fig. 17). The BHJ blend exhibits a homogeneous composite morphology, as evidenced by the atomic force microscopy (AFM) results shown in Supplementary Fig. 18. By analyzing the mechanical properties, including modulus and adhesion, the two components can be distinguished: TiO_2 domains exhibit higher stiffness, whereas PPy shows stronger adhesion. The relatively uniform distribution of these mechanical contrasts across the surface indicates a well-dispersed and homogeneous composite structure.

4.3 Characterizations: The Scanning electron microscope (SEM) measurement was carried out on a Carl Zeiss Supra 55 scanning electron microscope. Before the SEM examination, a layer of carbon was sputtered onto the sample surface. The microscopic images were obtained on the Leica DM4000M fluorescence microscope. The TEM measurement was performed on a FEI Talos X-FEG microscope. The TEM sample was prepared by applying the sample onto a carbon coated copper grid. UV-Vis measuremnets were carried out on a Lambda 750f Spectrometer. The TGA was performed on the Mettler Toledo TGA thermal gravimetric analyzer by heating the sample placed in a platinum pan from 25˚C to 600˚C at a rate of 10 ˚C/min under air purge (30 mL/min). FTIR measurement was carried out on a Thermo Scientific Nicolet IS10 Fourier transform infrared spectrometer with the OMNIC software. Samples were

prepared by mixing 1 mg of the compound with 500 mg of KBr in a mortar and pressed under a pressure of 12 Pa for 2 min to form a pellet. AFM, C-AFM and KPFM measurements were carried out on a Bruker Dimension atomic force microscope. The energy gaps of the BHJ blend were determined from the UV-Vis-NIR spectra using the Tauc plot method. XANES data were collected at Beamline 14W at Shanghai Synchrotron Radiation Facility. The electrometer was conducted using Keithley electrometers (Models 6514 and 2400). PL spectra were obtained from the Applied Nanofluorescence Spectrometer (USA).

4.4 Light-driven levitation and propulsion of the PPy-TiO_2 BHJ blend: The motion of the blend placed on a A4 paper substrate was activated by applying the visible light (X-cite 120Q, Excelitas Technologies) from different angles at a distance of approximately 2 cm from the sample and recorded by a CCD camera or an ultra-high-speed camera (Phantom V310 high speed camera, which is capable of recording at a maximum of 500000 FPS). Unless otherwise mentioned, the visible light intensity and the volume ratio between TiO_2 and PPy inside the blend are fixed at 0.8 W/cm^2 and 1:1, respectively. An optical filter with the cutoff wavelength between 400 and 800 nm was utilized in order to avoid the over exposure of the cameras. PhysVis software was utilized to analyze the motion velocity.

4.5 Simulation of the PPy-TiO_2 BHJ blend for charge separation, diffusion and electrostatic repulsion force process: The density functional theory (DFT) calculations were performed using the Vienna Ab initio Simulation Package (VASP). PPy with three units were placed on the upper side of rutile TiO_2 (110) for non-excited

and one-electron removal by photoexcitation shown in Supplementary Fig. 19. In this work, we applied reducing one electron for the whole system (not designated to specific atom) to alternate the electron removal via photoexcitation. The Bader charge information for non-excited model and one-electron-deficiency model were shown in Supplementary Table 1 and 2, respectively. The total number of electrons in the non-excited model contains 1334 Bader charges, whereas the one-electron-deficiency model with 1333 Bader charges shown in Supplementary Table 3. In addition, the reduction of one electron is predominantly contributed by PPy component (73.488 charges in Supplementary Table 3, non-excited model contains 72.591 charges), revealing that PPy acts as the electron-donating species while TiO_2 gaining electron. It indicates a strong electron redistribution in one-electron-deficiency model and would generate relatively higher charge transfer from PPy to TiO_2.

A FEM simulation incorporating the electromagnetic wave and frequency domain was employed to investigate the current density and its surface distribution in the PPy-TiO_2 model under photoexcitation. This model was simplified to a two-dimensional rectangular geometry, with the PPy layer with P type doping positioned on the top side and the rutile TiO_2 layer with N type doping distributed on the bottom of the model, as shown in Supplementary Fig. 19.

The FEM simulations considered the effects of incident light with different wavelength from 460 nm to 540 nm on the electric field intensity and current distribution of the PPy-TiO_2 model. As shown in Fig. 3i, we selected incident illumination with wavelength around 500 nm, which has a current to optical power ratio

around 3.49 × 10^{-2} A/W at the upper surface. Furthermore, it demonstrates that visible light at 500 nm induces the maximum current density (6.16×10^{9} A/m^2) across the entire model. Its current density distribution illustrates in Supplementary Fig. 20 and this trend applies to light with any wavelength that excites electron transfer. In addition, the arrowheads in Fig. 3h indicate the direction of the current opposite to the direction of electron transfer, confirming the results of Bader charge analysis of DFT simulation.

The simulation of electrostatic repulsive force between the PPy-TiO_2 BHJ and substrate was carried out by FEM performed by COMOSL Multiphysics software. The electrostatic and solid mechanics physics interfaces together with the electromechanics multi-physics coupling were employed to this model for researching electrostatic repulsive force. First, according to data from KPFM, a 1.5 V potential difference was applied between the lower boundary of the BHJ and the upper boundary of the substrate, where one electrode was defined as a terminal and the other is grounded. This configuration established an electrostatic field in the gap region. The electric potential distribution was obtained by solving the charge conservation equation.

FEM solves the electric potential V in the entire region according to the electrostatic physics interface control equations which are usually in the form of charge conservation, that is,

$$\nabla \cdot D = \rho_V \tag{1}$$

$$E = -\nabla V \ . \tag{2}$$

In a 2D model that considers only the y-direction, Eq. 2 is often written as,

$$E = \frac{V_0}{l} \ , \tag{3}$$

where l represents the vertical distance between the BHJ and substrate (60 μm). Subsequently, the electrostatic repulsive force between BHJ and substrate is calculated according to the following equation:

$$F = \int_{\partial\Omega} dnT\, dS \ , \tag{4}$$

where T is the Maxwell stress tensor (0 for x and y direction, 1 for z direction), and S is the contact area between the BHJ and the substrate. The formulation of T is

$$T = \varepsilon(E_i E_j - \frac{1}{2}E^2 I) \ , \tag{5}$$

where the ε is permittivity of air (8.854×10^{-12} F/m) and I is the unit tensor with a value of 1. In a 2D model that considers only the y-direction, Eq. 4 is often written as,

$$T = \frac{1}{2}\varepsilon E^2 \ . \tag{6}$$

Combining Eq. 4 and Eq. 6, the electrostatic repulsive force can be calculated by the following equation:

$$F = \frac{1}{2}\varepsilon E^2 S \ . \tag{7}$$

In a 2D model, Eq. 7 is written as

$$F = \frac{1}{2}\varepsilon E^2 L \ , \tag{8}$$

where the L is the length of BHJ (800 μm). Combining Eq. 3 and Eq. 8, the electrostatic repulsive force can be calculated as 2.21 μN.

4.6 Optimization of the PPy-TiO_2 BHJ blend levitation performance under different conditions: First, as shown in Supplementary Fig. 21, the PPy-TiO_2 blend exhibits different levitation behavior on different substrates. The levitation behavior is stronger as the dielectric constant of substrate increases, which is the best on Polytetrafluoroethylene (PTFE) and disappears on conductive substrates. This effect is

because the substate with high dielectric constant has stronger ability to retain charge while conductive substrate cannot retain charge (Supplementary Fig. 7). Second, we have evaluated the influence of light intensity and wavelength on the levitation behavior. As can be seen from Supplementary Fig. 22, the levitation height increases with the decreasing wavelength. This is because the higher illumination energy input results in more significant charge separation and the stronger electrostatic repulsion force. Third, as shown in Supplementary Fig. 23, the PPy-TiO_2 blend with different PPy to TiO_2NP mass ratio shows different levitation height. The highest levitation height is observed when the volume ratio between PPy and TiO_2NP is 1:1, which is likely because of the enhanced charge transportation efficiency enabled by the connected charge percolation network in this case. Last, the levitation height is also affected by the thickness of the PPy-TiO_2 blend. As shown in Supplementary Fig. 8, the levitation height decreases with the increasing thickness of the PPy-TiO_2 blend. This is mainly due to the increased gravity of the blend.

Acknowledgments

This work is supported by the National Natural Science Foundation of China (22573070, 52503158), the Basic Research Program of Jiangsu (BK20250795), the Joint International Research Laboratory of Carbon-Based Functional Materials and Devices, the Key Projects of the Regional Joint Fund of the National Natural Science Foundation of China (U24A20496), the Gusu Innovation and Entrepreneurship Talent Program-Major Innovation Team (ZXD2023002), the Collaborative Innovation Center of Suzhou

Nano Science & Technology, the 111 Project, and the Suzhou Key Laboratory of Functional Nano & Soft Materials. It was also supported by the Priority Academic Program Development of Jiangsu Higher Education Institutions (PAPD), the Fund for Excellent Creative Research Teams of Jiangsu Higher Education Institutions, and the Suzhou Key Laboratory of Surface and Interface Intelligent Matter (SZS2022011).

Author contributions

D.W., C.Z., H.H., M.L., C.C., J.W., H.Z., B.D., and M.S. proposed and designed the research. D.W., C.Z., H.H., M.L., J.W., H.Z., W.P., and J. Z. performed the experiments and analyzed the data. X.F. built the control platform. C.Z. and H.Y. conducted the model analysis. L.L., H. Z. conducted the AFM experiments. B.D. and M.S. supervised the research. All authors discussed the results and wrote the manuscript.

Competing interests

The authors declare that they have no competing interests.

Data and materials availability

All data needed to evaluate the conclusions in the paper are present in the paper and/or the Supplementary Information.

References

1 Liu, Z., Wang, C., Ren, Z., Wang, C., Wang, W., Ko, J., Song, S., Hong, C., Chen, X., Wang, H., Hu, W. & Sitti, M. 3D-printed low-voltage-driven ciliary hydrogel microactuators. *Nature* **649**, 885-893 (2026).

2 Aubin, C. A., Heisser, R. H., Peretz, O., Timko, J., Lo, J., Helbling, E. F., Sobhani, S., Gat, A. D. & Shepherd, R. F. Powerful, soft combustion actuators for insect-scale robots. *Science* **381**, 1212-1217 (2023).

3 Wang, D. L., Liu, Z., Zhao, H., Qin, H., Bai, G., Chen, C., Shi, P., Du, Y., Zhao, Y., Liu, W., Wang, D., Zhou, G., He, X. & Dai, C. Launching by cavitation. *Science* **389**, 935-939 (2025).

4 Zhang, Y., Pan, C., Liu, P., Peng, L., Liu, Z., Li, Y., Wang, Q., Wu, T., Li, Z.,

Majidi, C. & Jiang, L. Coaxially printed magnetic mechanical electrical hybrid structures with actuation and sensing functionalities. *Nat. Commun.* **14**, 4428 (2023).

5 Johnson, B. K., Naris, M., Sundaram, V., Volchko, A., Ly, K., Mitchell, S. K., Acome, E., Kellaris, N., Keplinger, C., Correll, N., Humbert, J. S. & Rentschler, M. E. A multifunctional soft robotic shape display with high-speed actuation, sensing, and control. *Nat. Commun.* **14**, 4516 (2023).

6 Shi, Z., Zhang, Z., Schnermann, J., Neuhauss, S. C. F., Nama, N., Wittkowski, R. & Ahmed, D. Ultrasound-driven programmable artificial muscles. *Nature* **646**, 1096-1104 (2025).

7 Feng, M., Yang, D., Ren, L., Wei, G. & Gu, G. Y. X-crossing pneumatic artificial muscles. *Sci. Adv.* **9**, eadi7133 (2023).

8 Li, M., Tang, Y., Soon, R. H., Dong, B., Hu, W. & Sitti, M. Miniature coiled artificial muscle for wireless soft medical devices. *Sci. Adv.* **8**, eabm5616 (2022).

9 Bao, X., Wang, F., Zhang, J., Li, M., Zhang, S., Ren, Z., Liao, J., Yan, Y., Kang, W., Zhang, R., Liu, Z., Wang, T. & Sitti, M. Real-time in situ magnetization reprogramming for soft robotics. *Nature* **645**, 375-384 (2025).

10 Li, M., Pal, A., Aghakhani, A., Pena-Francesch, A. & Sitti, M. Soft actuators for real-world applications. *Nat. Rev. Mater.* **7**, 235-249 (2022).

11 Yang, Q., Liu, T. L., Xue, Y., Wang, H., Xu, Y., Emon, B., Wu, M., Rountree, C., Wei, T., Kandela, I., Haney, C. R., Brikha, A., Stepien, I., Hornick, J., Sponenburg, R. A., Cheng, C., Ladehoff, L., Chen, Y., Hu, Z., Wu, C., Han, M., Torkelson, J. M., Kozorovitskiy, Y., Saif, M. T. A., Huang, Y., Chang, J. K. & Rogers, J. A. Ecoresorbable and bioresorbable microelectromechanical systems. *Nat. Electron.* **5**, 526-538 (2022).

12 Ha, K. H., Yoo, J., Li, S., Mao, Y., Xu, S., Qi, H., Wu, H., Fan, C., Yuan, H., Kim, J. T., Flavin, M. T., Yoo, S., Shahir, P., Kim, S., Ahn, H. Y., Colgate, E., Huang, Y. & Rogers, J. A. Full freedom-of-motion actuators as advanced haptic interfaces. *Science* **387**, 1383-1390 (2025).

13 Bai, H., Zhou, J., Wu, M., Papastefan, S., Li, X., Zhang, H., Zhao, K., Zhang, Z., Ouyang, W., Redden, C. R., Alhajjat, A. M., Wang, H., Zhou, Y., Madsen, K., Li, S., Efimov, A. I., Ma, K., Kovacs, L., Patel, S., Liesman, D. R., Ott, K. C., Garziera, R., Sammet, S., Zhang, W., Huang, Y., Shaaban, A. F. & Rogers, J. A. A filamentary soft robotic probe for multimodal in utero monitoring of fetal health. *Nat. Biomed. Eng.*, DOI: 10.1038/s41551-41025-01605-41553 (2026).

14 Liu, Y., Zhou, Y., Qin, H., Yang, T., Chen, X., Li, L., Han, Z., Wang, K., Zhang, B., Lu, W., Chen, L. Q., Bernholc, J. & Wang, Q. Electro-thermal actuation in percolative ferroelectric polymer nanocomposites. *Nat. Mater.* **22**, 873-879 (2023).

15 Wu, S., Baker, G. L., Yin, J. & Zhu, Y. Fast thermal actuators for soft robotics. *Soft Robot.* **9**, 1031-1039 (2022).

16 Tiryaki, M. E., Elmacıoğlu, Y. G. & Sitti, M. Magnetic guidewire steering at ultrahigh magnetic fields. *Sci. Adv.* **9**, eadg6438 (2023).

17 Wang, C., Wang, T., Li, M., Zhang, R., Ugurlu, H. & Sitti, M. Heterogeneous

multiple soft millirobots in three-dimensional lumens. *Sci. Adv.* **10**, eadq1951 (2024).

18 Hong, C., Wu, Y., Wang, C., Ren, Z., Wang, C., Liu, Z., Hu, W. & Sitti, M. Wireless flow-powered miniature robot capable of traversing tubular structures. *Sci. Robot.* **9**, eadi5155 (2024).

19 Conrad, S., Teichmann, J., Auth, P., Knorr, N., Ulrich, K., Bellin, D., Speck, T. & Tauber, F. J. 3D-printed digital pneumatic logic for the control of soft robotic actuators. *Sci. Robot.* **9**, eadh4060 (2024).

20 Paikar, A., Novichkov, A. I., Hanopolskyi, A. I., Smaliak, V. A., Sui, X., Kampf, N., Skorb, E. V. & Semenov, S. N. Spatiotemporal regulation of hydrogel actuators by autocatalytic reaction networks. *Adv. Mater.* **34**, 2106816 (2022).

21 Kim, Y., Yuk, H., Zhao, R., Chester, S. A. & Zhao, X. Printing ferromagnetic domains for untethered fast-transforming soft materials. *Nature* **558**, 274-279 (2018).

22 Alapan, Y., Karacakol, A. C., Guzelhan, S. N., Isik, I. & Sitti, M. Reprogrammable shape morphing of magnetic soft machines. *Sci. Adv.* **6**, eabc6414 (2020).

23 Hu, W., Lum, G. Z., Mastrangeli, M. & Sitti, M. Small-scale soft-bodied robot with multimodal locomotion. *Nature* **554**, 81-85 (2018).

24 Yao, D. R., Kim, I., Yin, S. & Gao, W. Multimodal soft robotic actuation and locomotion. *Adv. Mater.* **36**, 2308829 (2024).

25 Landers, F. C., Hertle, L., Pustovalov, V., Sivakumaran, D., Oral, C. M., Brinkmann, O., Meiners, K., Theiler, P., Gantenbein, V., Veciana, A., Mattmann, M., Riss, S., Gervasoni, S., Chautems, C., Ye, H., Sevim, S., Flouris, A. D., Puigmartí-Luis, J., Mayor, T. S., Alves, P., Lühmann, T., Chen, X., Ochsenbein, N., Moehrlen, U., Schubert, T., Kulcsar, Z., Gruber, P., Weisskopf, M., Boehler, Q., Pané, S. & Nelson, B. J. Clinically ready magnetic microrobots for targeted therapies. *Science* **390**, 710-715 (2025).

26 Liu, X., Wang, L., Xiang, Y., Liao, F., Li, N., Li, J., Wang, J., Wu, Q., Zhou, C., Yang, Y., Kou, Y., Yang, Y., Tang, H., Zhou, N., Wan, C., Yin, Z., Yang, G. Z., Tao, G. & Zang, J. Magnetic soft microfiberbots for robotic embolization. *Sci. Robot.* **9**, eadh2479 (2024).

27 Wang, T., Ugurlu, H., Yan, Y., Li, M., Li, M., Wild, A. M., Yildiz, E., Schneider, M., Sheehan, D., Hu, W. & Sitti, M. Adaptive wireless millirobotic locomotion into distal vasculature. *Nat. Commun.* **13**, 4465 (2022).

28 Gonzalez-Ballestero, C., Aspelmeyer, M., Novotny, L., Quidant, R. & Romero-Isart, O. Levitodynamics: Levitation and control of microscopic objects in vacuum. *Science* **374**, eabg3027 (2021).

29 Schafer, B. C., Kim, J., Sharipov, F., Hwang, G. S., Vlassak, J. J. & Keith, D. W. Photophoretic flight of perforated structures in near-space conditions. *Nature* **644**, 362-369 (2025).

30 Does, M., Knippertz, P., Zschenderlein, P., Harrison, R. G. & Stuut, J. B. W. The mysterious long-range transport of giant mineral dust particles. *Sci. Adv.* **4**, eaau2768 (2018).

31 Ge, S., Nemiroski, A., Mirica, K. A., Mace, C. R., Hennek, J. W., Kumar, A. A. & Whitesides, G. M. Magnetic levitation in chemistry, materials science, and biochemistry. *Angew. Chem. Int. Ed.* **59**, 17810 (2020).
32 Kim, J. H., Pyo, J. B. & Kim, T. S. Highly mobile levitating soft actuator driven by multistimuli-responses. *Adv. Mater. Interfaces* **7**, 2001051 (2020).
33 Marzo, A., Seah, S. A., Drinkwater, B. W., Sahoo, D. R., Long, B. & Subramanian, S. Holographic acoustic elements for manipulation of levitated objects. *Nat. Commun.* **6**, 8661 (2015).
34 Melo, B., Cuairan, M. T., Tomassi, G. F. M., Meyer, N. & Quidant, R. Vacuum levitation and motion control on chip. *Nat. Nanotechnol.* **19**, 1270-1276 (2023).
35 Ilic, O. & Atwater, H. A. Self-stabilizing photonic levitation and propulsion of nanostructured macroscopic objects. *Nat. Photonics* **13**, 289-295 (2019).
36 Levchenko, I., Bazaka, K., Mazouffre, S. & Xu, S. Prospects and physical mechanisms for photonic space propulsion. *Nat. Photonics* **12**, 649-657 (2018).
37 Azadi, M., Popov, G. A., Lu, Z., Eskenazi, A. G., Bang, A. J. W., Campbell, M. F., Hu, H. & Bargatin, I. Controlled levitation of nanostructured thin films for sun-powered near-space flight. *Sci. Adv.* **7**, eabe1127 (2021).
38 Rieser, J., Ciampini, M. A., Rudolph, H., Kiesel, N., Hornberger, K., Stickler, B. A., Aspelmeyer, M. & Delić, U. Tunable light-induced dipole-dipole interaction between optically levitated nanoparticles. *Science* **377**, 987-990 (2022).
39 Poletkin, K. V., Asadollahbaik, A., Kampmann, R. & Korvink, J. G. Levitating micro-actuators: A review. *Actuators* **7**, 17 (2018).
40 Bustamante, C. J., Chemla, Y. R., Liu, S. & Wang, M. D. Optical tweezers in single-molecule biophysics. *Nat. Rev. Methods Primers* **1**, 25 (2021).
41 Grier, D. G. A revolution in optical manipulation. *Nature* **424**, 810-816 (2003).
42 Neuman, K. C. & Nagy, A. Single-molecule force spectroscopy: optical tweezers, magnetic tweezers and atomic force microscopy. *Nat. Methods* **5**, 491-505 (2008).
43 Yanagi, R., Takemoto, R., Ono, K. & Ueno, T. Light-induced levitation of ultralight carbon aerogels via temperature control. *Sci. Rep.* **11**, 12413 (2021).
44 Cortes, J., Stanczak, C., Azadi, M., Narula, M., Nicaise, S. M., Hu, H. & Bargatin, I. Photophoretic levitation of macroscopic nanocardboard plates. *Adv. Mater.* **32**, 1906878 (2020).
45 Grätzel, M. Photoelectrochemical cells. *Nature* **414**, 338-344 (2001).
46 Polman, A., Knight, M., Garnett, E. C., Ehrler, B. & Sinke, W. C. Photovoltaic materials: Present efficiencies and future challenges. *Science* **352**, aad4424 (2016).
47 Han, J., Xu, H., Corzo, D., Sharma, A. & Baran, D. Pathways to commercially viable organic photovoltaic materials. *Nat. Mater.*, DOI: 10.1038/s41563-41026-02501-41560 (2026).
48 Xie, Z., Liu, D., Gao, C., Dong, H. & Hu, W. High-mobility emissive organic semiconductors: an emerging class of multifunctional materials. *Nat. Rev. Mater.* **9**, 837-839 (2024).

49 Li, Y., Meng, N., Xu, Y., Yu, B., Liu, J., Cui, Y., Wang, Z., Ke, X., Pan, T., Min, X., Chen, J., Ma, D., Chao, L., Hu, Z., Xia, Y., Guo, Q., Chen, Y. & Huang, W. Sequential layer-by-layer deposition for high-performance fully thermal-evaporated red perovskite light-emitting diodes. *Nat. Commun.* **16**, 6908 (2025).

50 Han, P. & Zhang, Y. Recent advances in carbazole-based self-assembled monolayer for solution-processed optoelectronic devices. *Adv. Mater.* **36**, 2405630 (2024).

51 Ha, S. T., Li, Q., Yang, J. K. W., Demir, H. V., Brongersma, M. L. & Kuznetsov, A. I. Optoelectronic metadevices. *Science* **386**, eadm7442 (2024).

52 Huang, Y., Cui, Y., Deng, H., Wang, J., Hong, R., Hu, S., Hou, H., Dong, Y., Wang, H., Chen, J., Li, L., Xie, Y., Sun, P., Fu, X., Yin, L., Xiong, W., Shi, S. H., Luo, M., Wang, S., Li, X. & Sheng, X. Bioresorbable thin-film silicon diodes for the optoelectronic excitation and inhibition of neural activities. *Nat. Biomed. Eng.* **7**, 486-498 (2023).

53 Baharfar, M., Hillier, A. C. & Mao, G. Charge-transfer complexes: Fundamentals and advances in catalysis, sensing, and optoelectronic applications. *Adv. Mater.* **36**, 2406083 (2024).

54 Li, X., Aftab, S., Mukhtar, M., Kabir, F., Khan, M. F., Hegazy, H. H. & Akman, E. Exploring nanoscale perovskite materials for next-generation photodetectors: A comprehensive review and future directions. *Nano-Micro Lett.* **17**, 28 (2024).

55 Wang, Z. L. & Wang, A. C. On the origin of contact-electrification. *Mater. Today* **30**, 34-51 (2019).

56 Dong, X., Xiao, B., Vu, H., Lin, H. Z. & Sitti, M. Millimeter-scale soft capsules for sampling liquids in fluid-filled confined spaces. *Sci. Adv.* **10**, eadp2758 (2024).

57 Fan, X., Chen, Q., Li, M., Wu, Z., Tong, D., Xie, H., Yang, Z., Sun, L. & Sitti, M. Machining swarf formation-inspired fabrication of ferrofluidic helical miniature robots with multimodal locomotion capability. *Sci. Adv.* **11**, eads4411 (2025).

58 Andrade, M. A. B., Pérez, N. & Adamowski, J. C. Review of progress in acoustic levitation. *Braz. J. Phys.* **48**, 190-213 (2018).

59 Ashkin, A. & Dziedzic, J. M. Optical levitation by radiation pressure. *Appl. Phys. Lett.* **19**, 283-285 (1971).

60 Chang, W., Kim, J., Kim, M., Lee, M. W., Lim, C. Y., Kim, G., Hwang, S., Chang, J., Min, Y. H., Jeon, K., Kim, S., Choi, Y. H. & Lee, J. S. Concurrent self-assembly of RGB microLEDs for next-generation displays. *Nature* **617**, 287-291 (2023).

61 Hwang, J., Kim-Lee, H. J., Hong, S. W., Park, J. Y., Kim, D. K., Kim, D. H., Song, S., Jeong, J., Kim, Y., Yeom, M. J., Yu, M., Kim, J., Park, Y., Shin, D. C., Kang, S. S., Shin, J. K., Kim, Y., Yoon, E., Lee, H., Yoo, G., Jeong, J. & Hwang, K. Wafer-scale alignment and integration of micro-light-emitting diodes using engineered van der Waals forces. *Nat. Electron.* **6**, 216-224 (2023).

62 Behrman, K. & Kymissis, I. Micro light-emitting diodes. *Nat. Electron.* **5**, 564-573 (2022).

63 Lee, D., Cho, S., Park, C., Park, K. R., Lee, J., Nam, J., Ahn, K., Park, C., Jeon, K., Yuh, H., Choi, W., Lim, C. H., Kwon, T., Min, Y. H., Joo, M., Choi, Y. H., Lee, J. S., Kim, C. & Kwon, S. Fluidic self-assembly for MicroLED displays by controlled viscosity. *Nature* **619**, 755-760 (2023).

64 Karakuzu, B., Anil İnevi, M., Tarim, E. A., Sarigil, O., Guzelgulgen, M., Kecili, S., Cesmeli, S., Koc, S., Baslar, M. S., Oksel Karakus, C., Ozcivici, E. & Tekin, H. C. Magnetic levitation-based miniaturized technologies for advanced diagnostics. *Emergent Mater.* **7**, 2323-2348 (2024).

65 Yang, S., Rufo, J., Chen, Y., Chen, C., Drinkwater, B. W., Lee, L. P. & Huang, T. J. Acoustic tweezers for advancing precision biology and medicine. *Nat. Rev. Method Prim.* **5**, 49 (2025).

66 Geim, A. K., Simon, M. D., Boamfa, M. I. & Heflinger, L. O. Magnet levitation at your fingertips. *Nature* **400**, 323-324 (1999).

Supplementary Files

This is a list of supplementary files associated with this preprint. Click to download.

- SupplementaryInformation.docx
- SupplementaryVideos122.rar